Journal of Electronic Materials (2023) 52:5901–5910
https://doi.org/10.1007/s11664-023-10482-y

ORIGINAL RESEARCH ARTICLE

Cerium-Doped Bi_2S_3 Thin Films Fabricated by Nebulizer-Assisted Spray Pyrolysis Method for Photodetector Applications

V. Ganesh[1] · **I. S. Yahia**[1]

Received: 9 September 2022 / Accepted: 24 April 2023 / Published online: 10 June 2023
© The Minerals, Metals & Materials Society 2023

Abstract

In this study, the performances of highly sensitive Ce-doped Bi_2S_3 thin film-based photodetectors is discussed. The Bi_2S_3:Ce thin films were successfully coated by using the nebulizer spray pyrolysis method on glass substrates with varying Ce concentrations of 0%, 2%, 4%, 6%, and 8%. Furthermore, the physical properties such as crystalline size, morphology and optical response of Bi_2S_3:Ce thin films were investigated through x-ray diffraction (XRD), field-emission scanning electron microscopy (FESEM), atomic force microscopy, optical absorption spectrophotometry, and photoluminescence spectroscopy (PL). The XRD study showed that 4% Ce-doped Bi_2S_3 film shows higher crystallinity. UV–visible studies showed that the absorption spectrum has a direct electronic transition with an energy gap of about 1.68 eV. The morphological studies revealed that the Bi_2S_3:Ce samples showed uniformly distributed nanoflakes. The 4% Ce-doped Bi_2S_3 film photodetector exhibited high responsivity (R) and detectivity (D^*) and showed a fast photoresponse for about 5 s and 2.6 s with the external quantum efficiency (EQE) of 435%, which makes it highly suitable as a high-performance photodetector.

Graphical Abstract

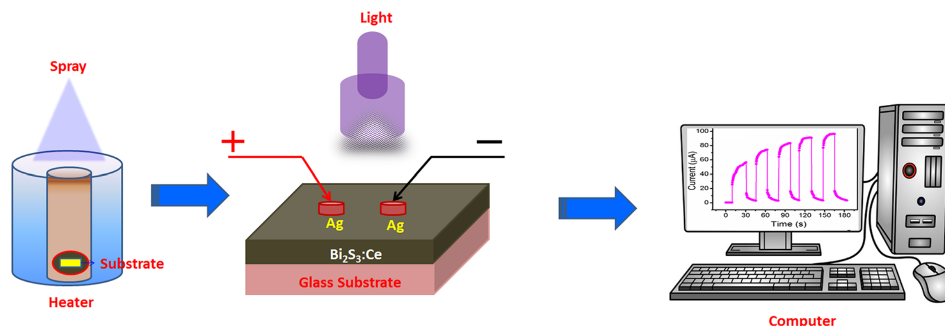

Keywords Bi_2S_3 thin film · Ce doping · nebulizer spray pyrolysis method · photodetector

Introduction

Optoelectronics is the study of electronic devices used to sense and regulate light sources. It converts the photons into electrical signals and photoresponsive devices include photodiodes, optical fibers, phototransistors, solar cells, etc. The photodetector is a type of photonic device that converts incident light or photons into electrical signals using the effect known as photoelectric conversion.[1] Therefore, the evolution of photodetectors towards photodetection utilization is based on progressive semiconducting materials and has been in the spectacular requirements of optoelectronic industries for device fabrication. They are also exploited for many applications, including space, photonics, communications, etc. Lead sulfide (PbS) based materials crop up as one of the most auspicious materials for photodetector

✉ V. Ganesh
vangaganesh@gmail.com

[1] Department of Physics, Faculty of Science, King Khalid University, P.O. Box 9004, Abha, Saudi Arabia

application, since they offer many assets, including low-cost manufacturing, solution processability, size-regulated spectral responsiveness, and malleable substrate compatibility in conventional photodetectors.[2] However, the toxicity of lead ions and the stability of perovskite materials are the two bottlenecks of lead halide-based perovskite in commercial applications.[3] Lead is one of the most challenging of toxic metals, and its analysis and disposal remain a serious health concern.[4] Hence, in order to replace lead, many new materials have been emerging to rival the performance of lead-based materials. Bismuth (Bi) is one of the less toxic materials that is being investigated as a semiconducting material because of its fascinating properties, such as tunable energy gap, larger carrier diffusion length, and mobility, making it better suited for a wide range of applications in injection laser diodes, solar cells, and optoelectronics.[5–11] Moreover, Bi possesses better optical properties which minimize the rate of recombination of the charge carriers generated because of the induced photons and has a better competence for incident light consumption.[12–14] All the aforementioned works have demonstrated different coating methods to develop Bi-based photodetectors and have suggested that Bi compounds have very good photodetection properties suitable for their application in optoelectronic devices. Similarly, Ce^{3+}ion-doped Cs_3MnBr_5 metal halide nanocrystals, showed an ample UV response, have a greatly boosted the photoluminescence quantum yield, enhanced responsivity, and built-in stability.[15] In the present work, Ce-doped Bi_2S_3 thin films were engineered using a nebulizer spray pyrolysis technique with varying Ce (0%, 2%, 4%, 6%, and 8%) concentrations. Spray pyrolysis is extensively used in laboratories to deposit thin films because of its simple manipulated technique, low cost, improved surface consistency, capability of managing particle shape and size, architecture of phase homogeneity of thin films, and the capability of producing large surface areas of high-quality thin films of uniform thickness, while adding dopants with the precursor solution in spray coating is simple compared to other techniques.[16,17] Hence, spray pyrolysis was adopted in this work to deposit Ce-doped Bi_2S_3 thin films with varying Ce (0%, 2%, 4%, 6%, and 8%) concentrations. The 4% Ce-doped Bi_2S_3thin film has shown the best improvement in responsivity, detectivity, and high external quantum efficiency (EQE).

Materials and Characterization

For a thin-film coating on the glass substrates, a solution was made by mixing 0.02 M of bismuth nitrate ($Bi_2(NO_3)_2$) and 0.03 M of thiourea in 10 mL distilled water. The solution pH was 5 and it was stirred for 10 minutes at room temperature. The glass substrates were cleaned to remove any impurities with hot chromic acid and rinsed several times using distilled water. A 10-mL volume of the solution was sprayed onto the glass substrates which were maintained at 300 °C with an applied pressure of about 1.5 kg/cm^2. The same methodology was repeated to prepare Ce-doped Bi_2S_3 thin films with various concentrations of cerium (III) nitrate hexahydrate with 0%, 2%, 4%, 6%, and 8% added to the starting water solvent solution, as shown in Fig. 1.

The average film thickness was calculated using a stylus profilometer, and it is found to be varied between 400 nm and 500 nm. The microstructural properties of the thin films were measured by an x-ray diffractometer (XRD) using CuKα radiation (λ = 1.5406 Å) with the flip-through angle (2θ) between 10° and 80°. The surface topologies of the thin films were studied using field-emission scanning electron microscopy (FESEM; Ultra 55; Carl Zeiss). The photo-emission studies were carried out through photoluminescence (PL) spectroscopy (Thermo Fisher spectrometer) with excitation λ_{exc} = 450 nm. UV–vis studies were recorded using a spectrophotometer (UV 1800; Shimadzu) within the

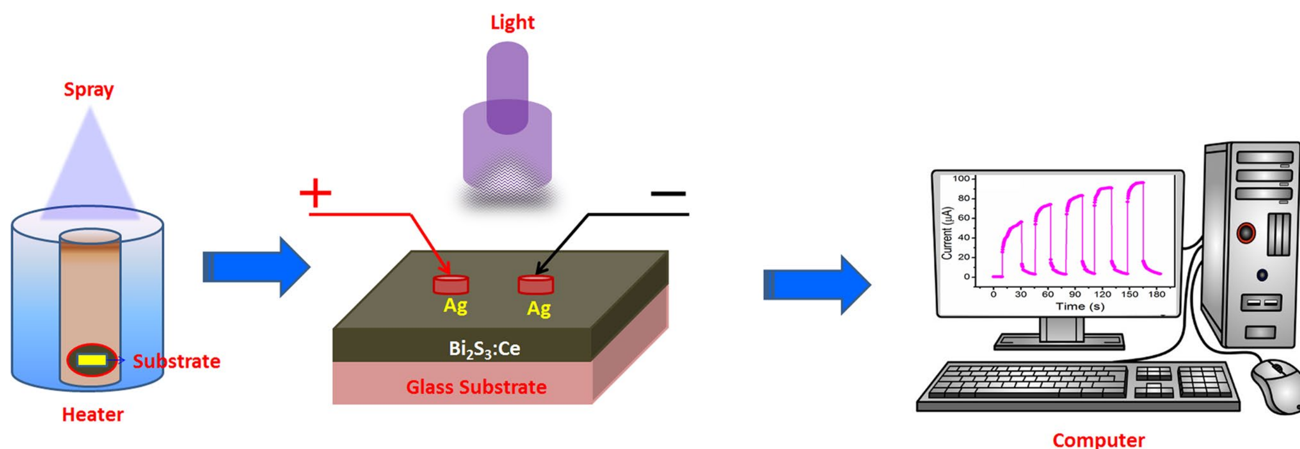

Fig. 1 Schematic of the preparation and device structure of Ce-doped Bi_2S_3 thin-film photodetector

wavelength range of 350–900 nm. The photosensing properties, such as responsivity, detectivity, and EQE, of the thin films were obtained using a source meter (2450; Keithley) accompanied by a laser source of wavelength 532 nm.

Results and Discussion

Structural and MicroStructural Properties

The XRD patterns of the Ce-doped (0%, 2%, 4%, 6%, and 8%) Bi_2S_3thin films are shown in Fig. 2, confirming that the diffraction patterns, (020), (120), (220), (101), (111), (211), (301), (410), (240), (420), (041), (411), (002), (501), (312), and (531) of Bi_2S_3:Ce thin films match the JCPDS card no 17–0320, and also belong to an orthorhombic structure with space group Pbnm (62). In addition, it was observed that there is an absence of a secondary phase or impurity peaks, which indicates that the Ce atom has integrated into the lattice as a substitution on the Bi_2S_3 host and not as an interstitial atom. Furthermore, a shift in the XRD peak of plane (111) was observed towards a lower 2θ value, due to the replacement of Bi^{3+} atoms with higher ionic radius Ce^{3+}atoms.[16] Similarly the intensity of plane (111) of the thin film increased with the increasing dopant percentage of Ce from 0% to 4% in the Bi_2S_3 host at a certain limit, and is directly correlated with the number of crystallites grown on the film. However, for a higher concentration Ce above 4–8%, the XRD peak of plane (111) shows a decrease in the intensity and broadening of the peak due to the reduction of the crystallite size. In addition, this change in crystallinity may affect the photodetector efficiency and time transient characteristics. High crystallinity leads to a low density of trap centers on their surfaces affecting their carrier mobility which improves the photoresponse.[18] Hence, the high crystallinity achieved for the 4% Ce-doped Bi_2S_3film offers a good photoresponse compared to the other dopant concentrations.

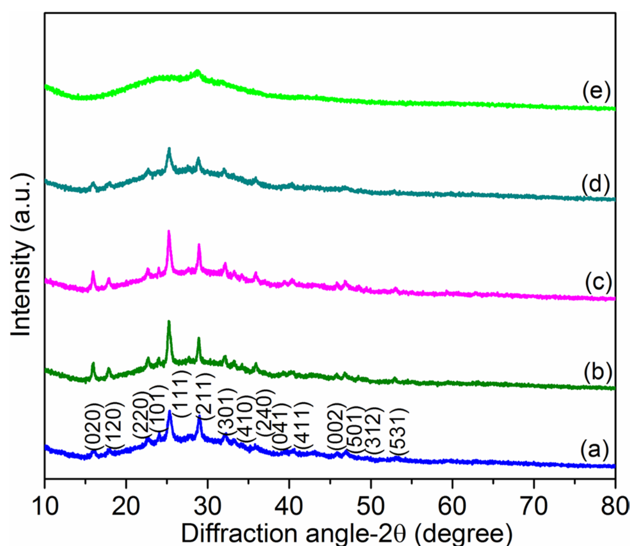

Fig. 2 XRD patterns of (a) 0%, (b) 2%, ©) 4%, (d) 6%, and (e) 8% Ce-doped Bi_2S_3 thin films

The lattice parameters, crystallite size, and strain of Ce-doped Bi_2S_3thin films with different doping concentrations were calculated, in which the lattice parameters of orthorhombic structure such as a, b, c were calculated by using Eq. (1), where d is the interplanar distance, Eq. (2) which is the volume of the unit cell (V), and Eq. (3) which is used to estimate the ε microstrain[19,20]

$$\frac{1}{d^2} = \left(\frac{h^2}{a^2} + \frac{k^2}{b^2} + \frac{l^2}{c^2}\right) \tag{1}$$

$$V = abc \tag{2}$$

$$\varepsilon = \frac{\beta \mathrm{Cot}\theta}{4} \tag{3}$$

The crystallite size D has been calculated using the full width at half-maximum of the preferential peak (111) of Bi_2S_3 using Scherrer's formula[21]:

$$D = \frac{0.9\lambda}{\beta \mathrm{Cos}\theta} \tag{4}$$

The measured values are tabulated in Table I, from which it can be seen that there are slight changes in the lattice constants compared to the standard values as a function of dopant concentration indicating that the Ce atoms are well incorporated into the crystal lattice of Bi_2S_3.[22] Similarly,

Table I Lattice constant, crystallite size, cell volume, and strain of Ce-doped Bi_2S_3 thin films

Samples	Crystallite size (nm)	Strain × 10^{-3}	Lattice constants			Cell volume V (Å^3)
			a (Å)	b (Å)	c (Å)	
Bi_2S_3:Ce0%	46	3.42	11.36	3.99	11.25	511
Bi_2S_3:Ce2%	64	2.49	11.38	4.00	11.27	514
Bi_2S_3:Ce 4%	71	2.22	11.24	3.98	11.55	516
Bi_2S_3:Ce 6%	56	2.83	11.32	4.00	11.28	511
Bi_2S_3:Ce 8%	51	3.06	11.20	3.89	11.31	490

the cell volume changes with the function of the doping concentration, due to Ce atoms with differences of valence level and electronegativity, as shown in Table I.[23]

From the XRD patterns, it was noticed that the diffraction peaks become narrowed as the Ce concentration is increased, indicating an increment in the crystallite size.[24] Therefore, it has been inferred that, with the Ce concentrations from 0% to 4%, there is an increase of crystallite size from 46 nm to 71 nm, while, with further increases of Ce concentrations of 6% and 8%, the crystallite size is reduced from 56 nm to 51 nm.[25] A similar trend was reported by Demir et al. for Cu-doped Bi_2S_3 nanocomposites. The dopant Cu reduced the crystallite size of the Bi_2S_3 samples from 25 nm to 22 nm and enhanced the photocatalyst performance.[26] Arumugam et al. fabricated Ag-doped Bi_2S_3 thin films for photodiode application and found that the increment of the dopant increased the crystallite size from 16.08 nm to 20.02 nm. Riahi et al. revealed that an increasing depositing time and annealing temperature can increase the crystallite size, leading to high-quality crystalline films, which show excellent absorption in the visible region.[27] The decrease in crystallinity for the higher concentrations of the 6% and 8% doped samples may be due to the confinement of the Ce atoms in the grain boundaries, or due to the avalanche of active atoms during the deposition on the glass substrate.

UV–Vis Absorption Analysis

Figure 3a shows the variation absorption spectra of 0%, 2%, 4%, 6%, and 8% Ce-doped Bi_2S_3 thin films as a function of the wavelength range between 350 nm to 900 nm. It can be seen that the absorption peak of the Bi_2S_3 thin films increase with the increase in Ce doping concentration from 0% to 4%. This increase in absorption may be due to the increase in crystallite size.[28] The maximum absorbance is observed for the 4% Ce doped film for the wavelength ranges from 400 nm to 550 nm compared with other films. The maximum absorbance of incident photons leads to the transfer of more charge carriers in the lower energy state excited to the higher energy levels. Also, the absorption edge of the prepared thin films is shifted towards the higher wavelength region, or red shift, as the concentration of Ce dopants increases from 0% to 4%. This phenomenon could be due to the presence of minimal strain as a result of the Ce dopant in the Bi_2S_3 thin films. This type of red shift lowers the energy band (E_g) value. The optical band gaps (E_g) of the prepared samples were estimated through Tauc plots (Fig. 3b) according to[29]:

$$\alpha h\nu = A\left(h\nu - E_g\right)^{1/2} \tag{5}$$

where α indicates the absorption coefficient, h the Plank's constant, and ν the frequency of light radiation. As shown in Fig. 3b, the band gap is obtained from the linear

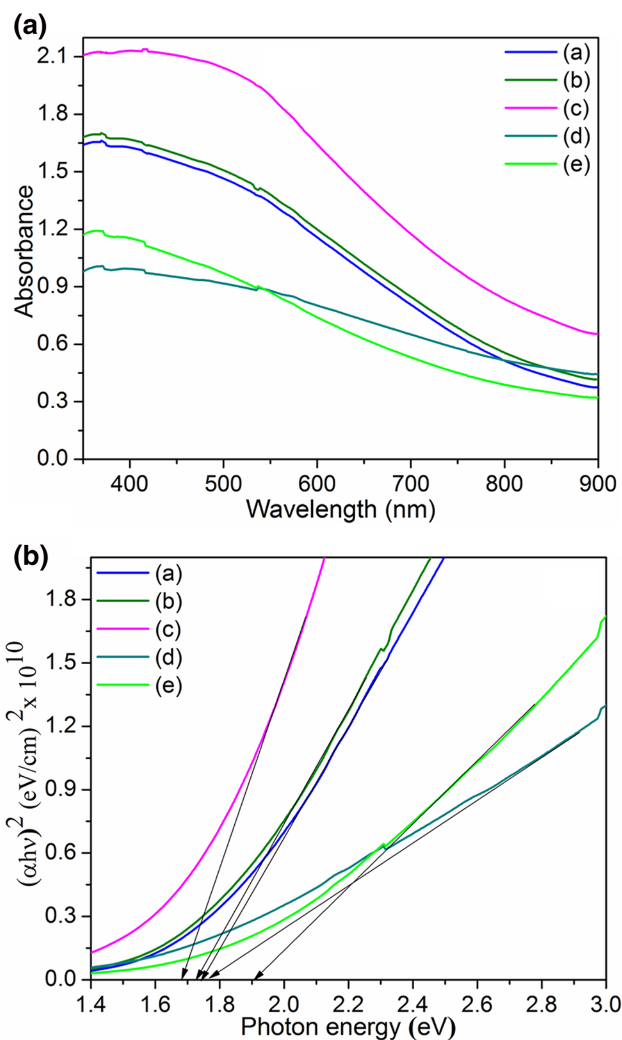

Fig. 3 (a) Absorbance spectra and (b) Tauc plot of (a) 0%, (b) 2%, (c) 4%, (d) 6%, and (e) 8% Ce-doped Bi_2S_3 thin films

extrapolation of the photon energy, Vs $(\alpha h\nu)^2$, for the direct band gap quantified for Ce-doped Bi_2S_3 thin films. The estimated energy gap value was found to be around 1.74 eV for undoped Bi_2S_3 thin film, and decreased from 1.74 eV to 1.68 eV with the increase of the Ce level from 0% to 4%. This is due to the fact that the presence of interstitial Bi atoms and more oxygen vacancies increases the concentration carriers and shifts the Fermi level to lower energies, although with a further increment in the concentration of the dopant, the absorption edge shifts towards the UV region, according to the Moss–Burstein effect.[30] Certainly, the Fermi level shifts above the conduction band with higher doping concentration. As a consequence, stuffing of the higher energy bands leads to absorptional transitions between the lower energy band and the Fermi level. Hence, this transitional level change shifts the edges of the absorptional peaks to higher energies.[31] The higher shift obtained

for the 4% Ce doping concentration is quantified as the least value of the energy band gap.[13]

Photoluminescence Studies

Figure 4 shows the PL spectra obtained for Ce-doped Bi_2S_3 thin films with the function of the Ce dopant levels at 0%, 2%, 4%, 6%, and 8% at room temperature. It shows that the luminescence sites occur in the wavelength range of about 475 nm to 525 nm for the dopant level varying from 0% to 8% of the Ce atoms which are associated with interlinearity of the Bi atoms. In this case, recombination of the excitons causes near-band edge emissions, which can be seen at 475 nm. Defects like oxygen vacancies generated by the sulfur content in Bi_2S_3 resulted in a green emission peak between the wavelengths of 500 nm and 525 nm. The inclusion of Ce in the Bi_2S_3hotspot has been shown to increase the strength of the green emission peak, which signals sulfur-induced oxygen vacancies when the Bi_2S_3 film is doped with 4% Ce. The augmentation of the Ce dopant to 8% resulted in no additional peak, which is in agreement with our XRD results. In contrast, the 8% Ce-doped Bi_2S_3 thin film's emission peak intensity decreased marginally when compared to the 4% Ce-doped thin film. The effect of surface area of the granules present on Ce-doped Bi_2S_3 thin films and the extrinsic defects roles on PL emissions were measured. When the photons reach the surface of the thin film, the lattice composition transforms with the contorted excited clusters, which allows the electrons to be captured, followed by the photons decaying by radiative or non-radiative transitions. These criteria enrich the light absorption and improve the charge carrier generation in the case of photodetectors.[32–34]

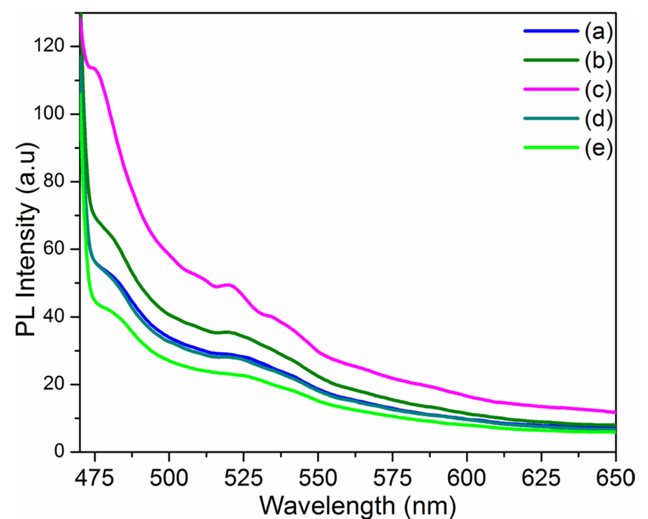

Fig. 4 Photoluminescence spectra of (a) 0%, (b) 2%, (c) 4%, (d) 6%, and (e) 8% Ce doped Bi_2S_3thin films

Morphological Studies

Figure 5 shows the FESEM images of the Ce doping at different level of 0%, 2%, 4%, 6%, and 8% on Bi_2S_3 thin films. It can be clearly seen that the surfaces of Ce-doped Bi_2S_3 thin films are covered by nanograins[28,35] and that the mean grain size grows with the increasing Ce dopant level. It can also be seen that the Ce doping at 2% and 4% shows films with irregular grains. The topology of the grains on the Bi_2S_3 thin films with Ce doping is slightly coarser than that of the undoped Bi_2S_3 host. Notably, grain boundaries amid the surface grains of the Bi_2S_3 thin film become visible and broad with an increase in the Ce dopant concentration. In another case, if the Ce doping level increased from 2% to 4%, the grain boundary states were filled, thereby increasing the average concentration of free carriers, resulting in a decrease of grain size. The surface of the Ce-doped Bi_2S_3 thin films became rougher with an increase in Ce concentration up to 4% and the film showed a better improvement, but when the dopant level increased to 6% and 8%, this made it less responsive to the light source compared to the 4% Ce-doped film.[36] An energy dispersive x-ray (EDX) spectrum of the 4% Ce-doped Bi_2S_3 thin film is shown in Fig. 5f, confirming the presence of Bi, S, and Ce elements in the sample. The atomic and weight percentage of the sample is shown in Fig. 5f.

Electrical Studies

The electrical conductivity of the Ce-doped Bi_2S_3 thin films was determined using the van der Pauw method. The measured values for the 0%, 1%, 2%, 3%, 4%, and 5% Ce-doped Bi_2S_3 thin films are 0.309 mho/cm, 0.415 mho/cm, 1.66 mho/cm, 0.748 mho/cm, and 1.01 mho/cm, respectively. Although the valence states of both Bi and Ce are 3 +, the increase in conductivity of the Bi_2S_3 thin films up to 4% might be because of the decreased energy gap of the samples and the increased crystalline size due to Ce doping. The decrement in the energy gap and the increased crystallite size leads to enhanced absorption of photons and reduced grain boundaries, respectively, causing more carriers to flow, enhancing the conductivity.[37–39] Furthermore, increasing the Ce dopant concentration beyond the optimal level causes the decrement in crystallite size and an enhanced band gap causing the electrical conductivity to decrease.

The photodetecting achievement of Ce (0%, 2%, 4%, 6% and 8%) doped on Bi_2S_3 nanoflakes and the *I–V* characteristics of the thin films were analyzed in both light OFF and light illumination of 1 mW/cm^2 to 5 mW/cm^2. Here, the Ag paste was used as a metal contact on the thin film, as shown in Fig. 6a. The applied bias across the electrodes was − 5

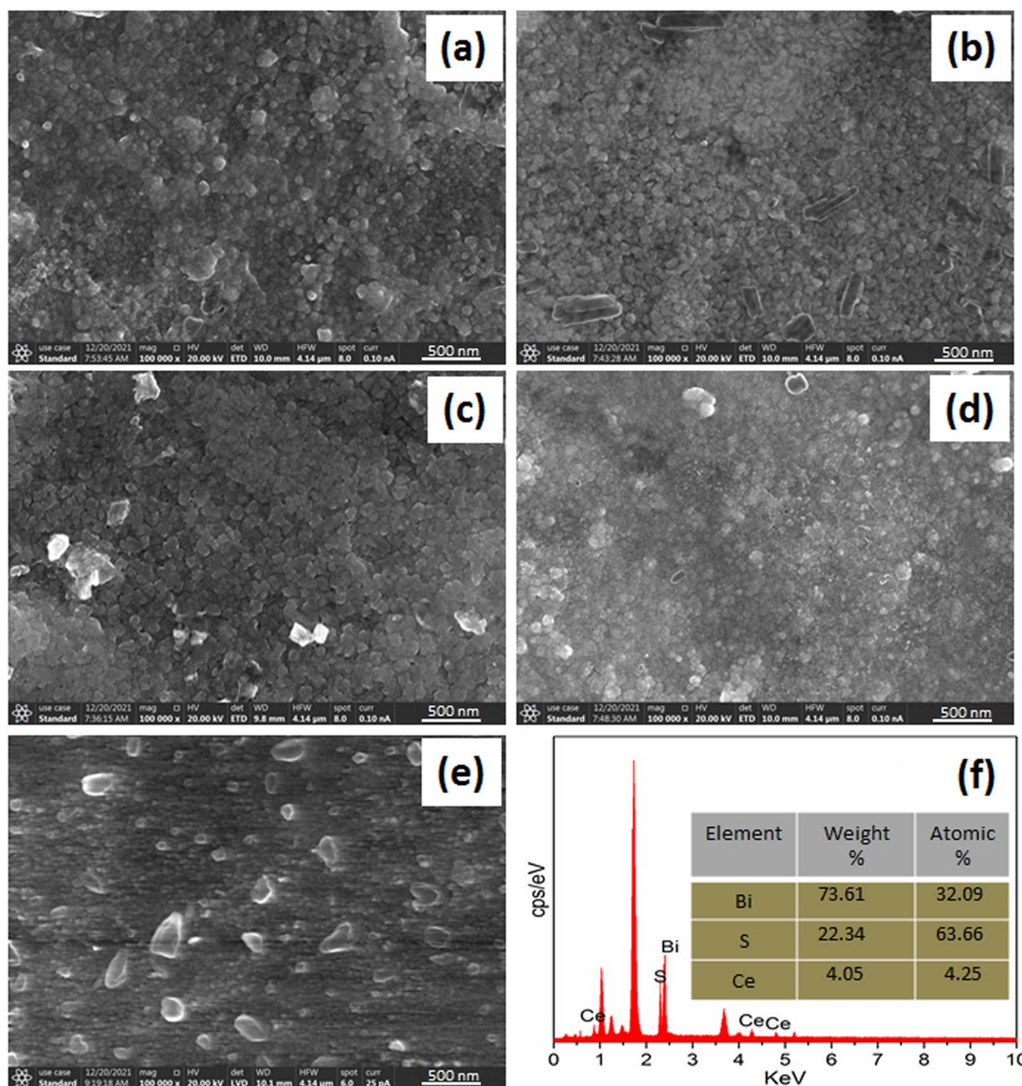

Fig. 5 FESEM images of (a) 0%, (b) 2%, (c) 4%, (d) 6%, and (e) 8% Ce-doped Bi_2S_3 thin films and (f) EDX pattern of Bi_2S_3:Ce 4% thin film

to + 5 V and the current flowing through the electrodes was noted. Figure 6b shows the *I–V* characteristics of the 0%, 2%, 4%, 6%, and 8% Ce-doped Bi_2S_3 thin films in dark and light modes. The *I–V* plot seems to be perfectly linear and symmetric on both the forward and reverse biasing conditions, confirming the formation ohmic contact.[40] The photocurrent response of all the thin films were considerably increased compared with the dark current. The Ce-doped Bi_2S_3 semiconductor covalent bonds were broken when the light shone on the thin films, allowing extra electron–hole pairs to enter and boost the current flowing through the films.[25] For the undoped Bi_2S_3 nanoflakes, the sulfur-induced oxygen vacancies contribute towards the flow of electrons, which are distributed on the surface of the Bi_2S_3 nanostructure and form a conduction platform for the electron flow using the formula: $O^{2-} \rightarrow V_O + 2e^-$. In the case of the 4% Ce-doped Bi_2S_3thin film, more electrons are generated by the higher concentration of the sulfur-induced oxygen vacancies.

The responsivity, EQE, and detectivity are the fundamental properties of photodetecting materials. Responsivity (*R*) is defined as the ratio of the induced photocurrent to the power of incident photons and the exposed area of the photodetector given by:

$$R = \frac{I_p}{P_{\text{in}} \times A} \tag{6}$$

$$D^* = R\sqrt{\frac{A}{2eI_d}} \tag{7}$$

where I_p, *A*, and *P* represent the photocurrent, active area, and power of the incident light, respectively.[6] Figure 7 , shows the comparative bar diagram between the detectivity,

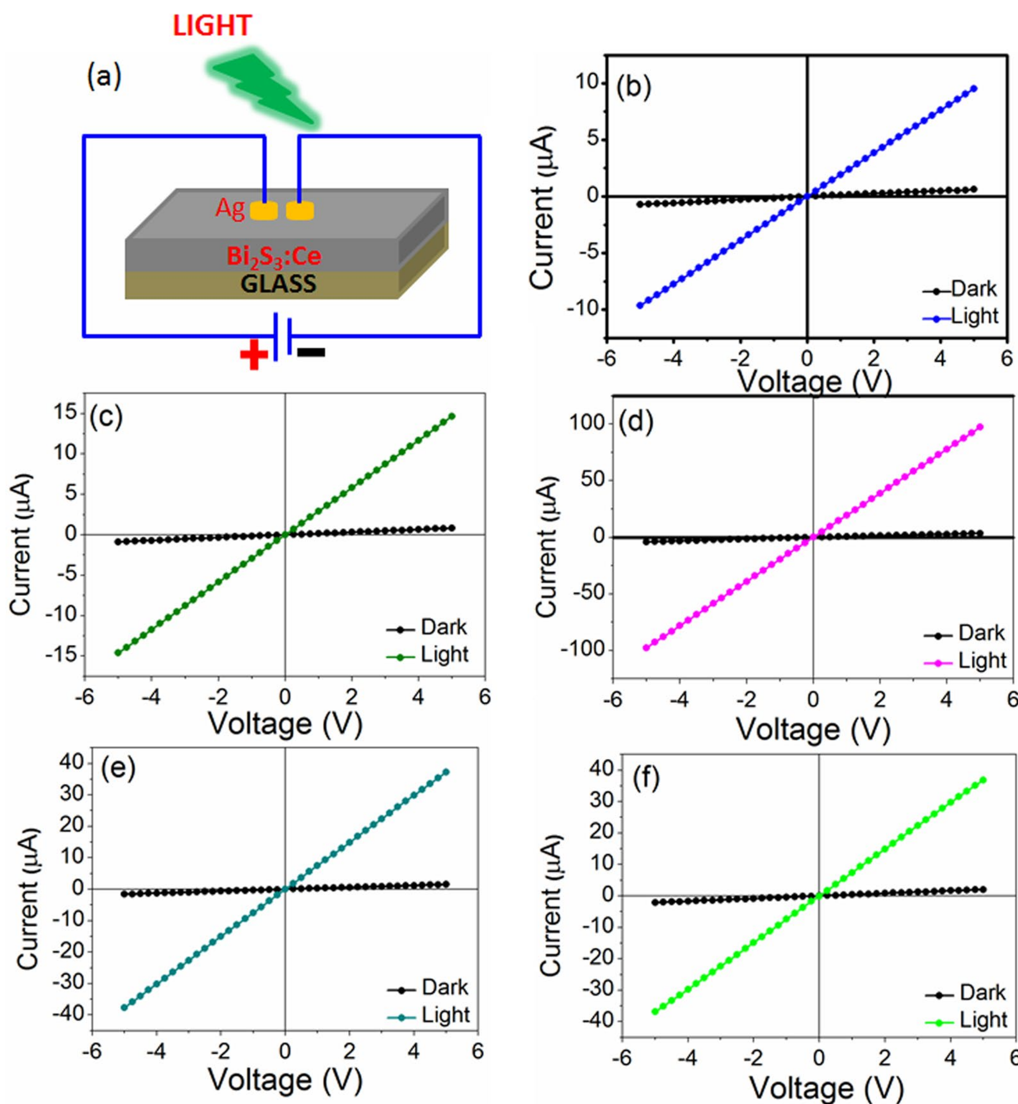

Fig. 6 (a) Schematic diagram and current vs voltage of (b) 0%, (c) 2%, (d) 4%, (e) 6%, and (f) 8% Ce-doped Bi_2S_3 thin films

EQE and responsivity, which clearly shows that Bi_2S_3:Ce nanoflakes of the Ce(4%)-Bi_2S_3 shows improved responsivity, detectivity, and high EQE compared to the other Ce dopant concentrations. The maximum responsivity value of 1.87 $AW^{-1}$for 4% Ce-doped Bi_2S_3 thin film (Table II) is higher than the Sm-doped PbS.[25] In the present work, the maximum detectivity is estimated as 5.73×10^{10}Jones for the 4% Ce-doped Bi_2S_3 thin film which is high compared to the polycrystalline $CH_3NH_3PbCl_3$ material.[41] The EQE, which is defined as the number of charge carriers detected per unit incident photon, is measured through [32]:

$$\text{EQE} = R\frac{hc}{e\lambda} \tag{8}$$

where h represents Planck's constant, c is the velocity of light, and λ is the wavelength of the laser light. Under the

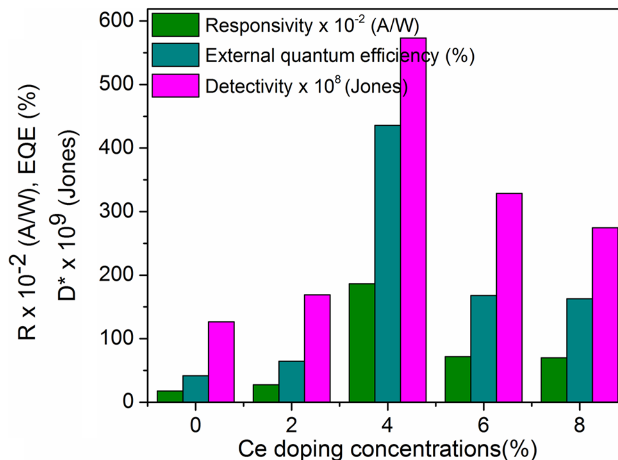

Fig. 7 Responsivity, EQE, and detectivity of Ce-doped Bi_2S_3 thin films

Table II Calculated values of responsivity, external quantum efficiency, detectivity, and rise and decay times of Ce-doped Bi_2S_3 thin films

Samples	R (AW^{-1})	EQE (%)	D^* (Jones)	Rise time (s)	Decay time (s)
Bi_2S_3:Ce0%	0.18	42	1.27×10^{10}	5.2	2.8
Bi_2S_3:Ce2%	0.28	64	1.69×10^{10}	5.0	2.7
Bi_2S_3:Ce 4%	1.87	435	5.73×10^{10}	5.0	2.6
Bi_2S_3:Ce 6%	0.72	168	3.29×10^{10}	5.1	2.8
Bi_2S_3:Ce 8%	0.69	163	2.74×10^{10}	5.3	2.7

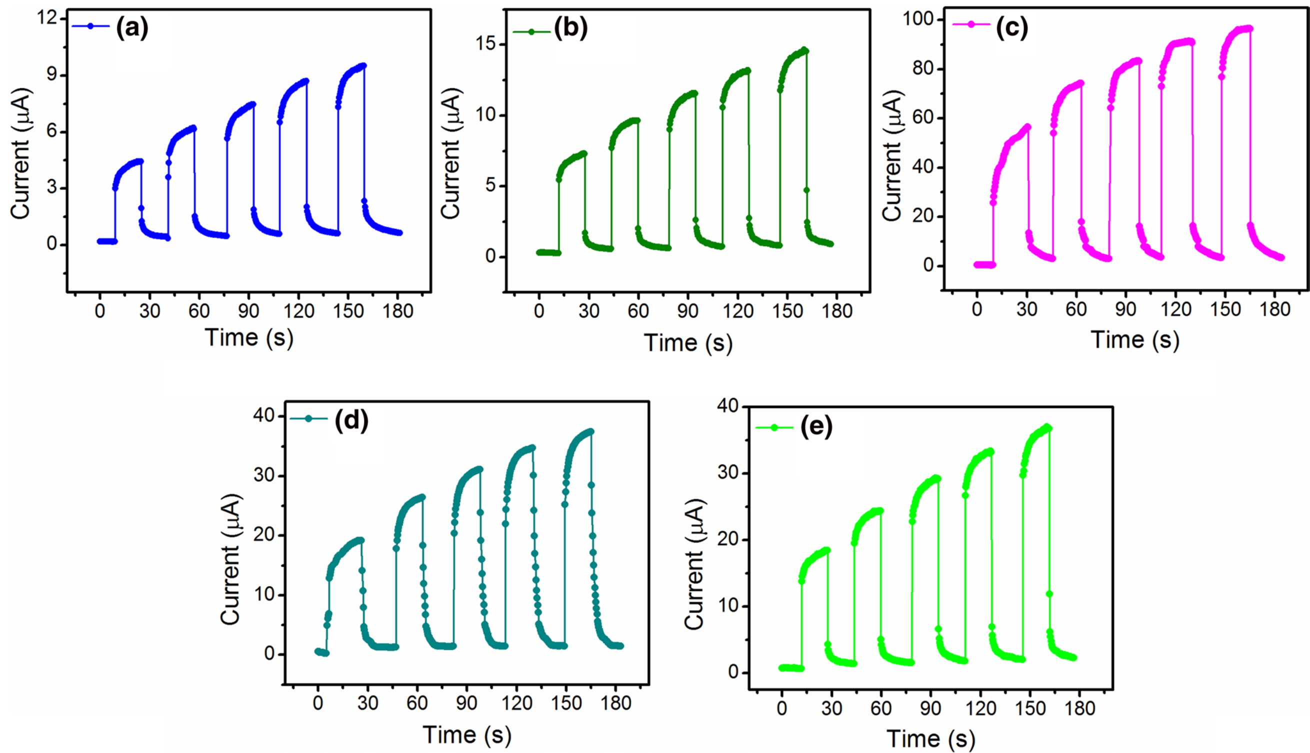

Fig. 8 Time versus current characteristics of (a) 0%, (b) 2%, (c) 4%, (d) 6%, and (e) 8% Ce-doped Bi_2S_3 thin films

Table III Comparison of the present work with previously reported works

Samples	Responsivity (A/W)	External quantum efficiency (EQE)	Detectivity (Jones)	Rise time (s)	Fall time (s)	Ref.
ZnO-Bi_2S_3	~ 1.23	–	–	–	–	[44]
Bi_2S_3 NRs/thin film	749.3×10^{-3}	–	5.61×10^{8}	162×10^{-3}	–	[45]
HGN/Bi_2S_3	1.09×10^{3}	–	2.78×10^{13}	–		[46]
Bi_2S_3/RuS_2	58.2×10^{-3}	78		0.4	0.7	[40]
Bi_2S_3 NW	2908.9	8.1×10^{3}	325×10^{11}	0.47×10^{-3}	0.94×10^{-3}	[47]
Bi_2S_3 NRs	–	–	–	0.8	3	[48]
2D Bi_2S_3 NSs	210×10^{-6}		3.75×10^{8}	0.1	0.1	[49]
Bi_2S_3:Ce4%	1.87	435	5.73×10^{10}	5.0	2.6	This work

biasing conditions, the Schottky barrier sinks and the depletion region shrinks, leading to the increased transfer efficiency of electrons to reach a high EQE.[42] The estimated EQE was 435%, which is higher than the value needed to achieve a high-sensitivity photodetector compared to earlier reported values.[40,43]

The time-dependent photoresponse behavior of the Ce-doped Bi_2S_3 thin films under a range of light intensities from 1 mW/cm^2 to 5 mW/cm^2 is shown in Fig. 8. Initially, the photocurrent is increased and reaches the saturation value under the exposure of light and starts decreasing rapidly to the dark current in the absence of light. The calculated rise and fall time values of different Ce concentrations of Bi_2S_3 thin films have been estimated and are tabulated in Table II. When the light was allowed to fall on the Bi_2S_3:Ce nanoflakes, the photocurrent surged to a point where it surpassed the point of saturation. When the light was turned off, the photocurrent returned to its starting value. The obtained amplitude of the peak had a rise time of about 5 s and a fall or decay time of 2.6 s in the case of the 4% Ce-doped Bi_2S_3 sample, which are better values compared to previously reported values.[25] Table III compares the photosensing parameter values of other Bi_2S_3-related samples. Moreover, the currently observed values for the 4% Ce-doped Bi_2S_3 sample being higher than previously reported samples maybe due to the large increase in the photocurrent, the grain boundary reduction, and the sulfur vacancies.[40,42–47]

The photosensing mechanism of Ce-doped Bi_2S_3 thin film is explained by the adsorption and desorption of oxygen molecules. An electrical depletion layer is formed when oxygen molecules are adsorbed by electrons on the surface of the Bi_2S_3 nanoflakes, which results in a reduction in conductivity. Electron–hole pairs are formed during the excitation of visible light on the surface of the Bi_2S_3:Ce thin films. The electrons attached to the oxygen molecules are recombined with these holes, and desorption occurs with the recovery of conductivity in the Ce-doped Bi_2S_3 thin films. The conductivity of a Ce-doped Bi_2S_3 thin film increases as a result of the desorption of more oxygen molecules from the film surface.[41,42] The conductivity of the samples is again reduced to initial values due to the adsorption of oxygen molecules.

Conclusions

From the XRD, it has been confirmed that Ce atoms are well incorporated in the Bi_2S_3 host material. The surface morphology of the thin films was studied by FESEM and a uniform grain distribution was observed for the 4% Ce-doped film. The band gap of Bi_2S_3:Ce 4% was tailored to reach 1.68 eV, which was evaluated from the absorbance spectra. The study revealed that nebulizer spray-coated Bi_2S_3:Ce4% film exhibit a better photoresponse, a high quantum efficiency, and high detectivity of 1.87 A/W, 435%, and 5.73×10^{10} Jones, respectively, which makes it a suitable candidate for the a photodetector, since bismuth and cerium are considered as less toxic materials, so that the fabricated thin films show an eco-friendly nature.

Acknowledgments The authors from King Khalid University (KKU) are grateful to the Deanship of Scientific Research at KKU for funding to carry this work through the research groups program under grant number R.G.P. 2/322/44.

Conflict of interest The authors declare that they have no known competing financial interests or personal relationships that could have appeared to influence the work reported in this paper. The authors declare that they have no conflict of interest.

References

1. S.S. Li, *Semiconductor Physical Electronics* (New York, NY: Springer, 2007), pp. 381–457.
2. R. Saran and R.J. Curry, *Nat. Photonics* 10, 81 (2016).
3. F. Igbari, Z.K. Wang, and L.S. Liao, *Adv. Energy Mater.* 9, 1803150 (2019).
4. W. Yantasee, Y. Lin, K. Hongsirikarn, G.E. Fryxell, R. Addleman, and C. Timchalk, *Environ. Health Perspect.* 115, 1683 (2007).
5. C.A. Hoffman, J.R. Meyer, F.J. Bartoli, A. Di Venere, X.J. Yi, C.L. Hou, H.C. Wang, J.B. Ketterson, and G.K. Wong, *Phys. Rev. B* 48, 11431 (1993).
6. Y. Guo, F. Pan, M. Ye, X. Sun, Y. Wang, J. Li, X. Zhang, H. Zhang, Y. Pan, Z. Song, J. Yang, and J. Lu, *ACS Appl. Mater. Interfaces* 9, 23128 (2017).
7. D.S. Choi, A.A. Balandin, M.S. Leung, G.W. Stupian, N. Presser, S.W. Chung, J.R. Heath, A. Khitun, and K.L. Wang, *Appl. Phys. Lett.* 89, 141503 (2006).
8. V. Chis, G. Benedek, P.M. Echenique, and E.V. Chulkov, *Phys. Rev. B Condens. Matter Mater. Phys.* 87, 075412 (2013).
9. Y. Yu, W. Wang, W. Li, G. Wang, Y. Wang, Z. Lu, S. Li, W. Zhao, Y. Li, T. Liu, and X. Yan, *Front. Chem.* 9, 832028 (2022).
10. C. Chen, H. Qiao, S. Lin, C. Man Luk, Y. Liu, Z. Xu, J. Song, Y. Xue, D. Li, J. Yuan, W. Yu, C. Pan, S. Ping Lau, and Q. Bao, *Sci. Rep.* 5, 11830 (2015).
11. J. Yin, Z. Tan, H. Hong, J. Wu, H. Yuan, Y. Liu, C. Chen, C. Tan, F. Yao, T. Li, Y. Chen, Z. Liu, K. Liu, and H. Peng, *Nat. Commun.* 9, 3311 (2018).
12. F. Reis, G. Li, L. Dudy, M. Bauernfeind, S. Glass, W. Hanke, R. Thomale, J. Schäfer, and R. Claessen, *Science* 357, 287 (2017).
13. M. Pumera and Z. Sofer, *Adv. Mater.* 29, 1605299 (2017).
14. H. Huang, X. Ren, Z. Li, H. Wang, Z. Huang, H. Qiao, P. Tang, J. Zhao, W. Liang, Y. Ge, J. Liu, J. Li, X. Qi, and H. Zhang, *Nanotechnology* 29, 235201 (2018).
15. L. Shao, D. Zhou, N. Ding, R. Sun, W. Xu, N. Wang, S. Xu, D. Liu, and H. Song, *ACS Sustain. Chem. Eng.* 9, 4980 (2021).
16. J. Arumugam, A. George, A. Dhayal Raj, A. Albert Irudayaraj, R.L. Josephine, S. John Sundaram, T. Saad Algarni, A.M. Al Mohaimeed, B. Balasubramanian, and K. Kaviyarasu, *Mater. Lett.* 302, 130403 (2021).
17. T. Sasikala, K. Shanmugasundaram, P. Thirunavukkarasu, J. Chandrasekaran, P. Vivek, R. Marnadu, M. Aslam Manthrammel, and S. Gunasekaran, *Inorg. Chem. Commun.* 130, 108701 (2021).

18. X.H. Nguyen, H.N. Luong, H.A. Pham, N.M. Nguyen, and V.Q. Dang, *RSC Adv.* 11, 36340 (2021).
19. R.S. Lokhande, S.R. Thakur, and P.A. Chate, *Optik (Stuttgart).* 219, 165230 (2020).
20. K.D. Arun Kumar, S. Valanarasu, A. Kathalingam, and K. Jeyadheepan, *Mater. Res. Bull.* 101, 264 (2018).
21. Z. Amara, M. Khadraoui, R. Miloua, A. Boukhachem, A. Ziouche, A. Nakrela, and A. Bouzidi, *Phys. B Condens. Matter* 585, 412121 (2020).
22. J. Arumugam, A. George, A.D. Raj, A.A. Irudayaraj, R.L. Josephine, S.J. Sundaram, A.M. Al-Mohaimeed, W.A. Al-onazi, M.S. Elshikh, and K. Kaviyarasu, *J. Alloys Compd.* 863, 2 (2021).
23. J. Molenda, A. Kulka, A. Milewska, W. Zajac, and K. Świerczek, *Materials (Basel)* 6, 1656 (2013).
24. C.W. Huang, B.J. Lin, H.Y. Lin, C.H. Huang, F.Y. Shih, W.H. Wang, C.Y. Liu, and H.C. Chui, *Nanoscale Res. Lett.* 7, 1 (2012).
25. K. Paulraj, S. Ramaswamy, N. Chidhambaram, H. Algarni, M. Shkir, and S. AlFaify, *Superlattices Microstruct.* 148, 106723 (2020).
26. H. Demir, Ö. Şahin, O. Baytar, and S. Horoz, *J. Mater. Sci. Mater. Electron.* 31, 10347 (2020).
27. M. Riahi, C. Martínez-Tomás, S. Agouram, A. Boukhachem, and H. Maghraoui-Meherzi, *Thin Solid Films* 626, 9 (2017).
28. H. Yue, S. Chen, P. Li, C. Zhu, X. Yang, T. Li, and Y. Gao, *Ionics (Kiel)* 25, 3587 (2019).
29. I.L.P. Raj, S. Valanarasu, S. Vinoth, N. Chidhambaram, R.S.R. Isaac, M. Ubaidullah, S.F. Shaikh, and B. Pandit, *Sens. Actuators A Phys.* 333, 113242 (2022).
30. N.R. Yogamalar and A. Chandra Bose, *Appl. Phys. A Mater. Sci. Process.* 103, 33 (2011).
31. Z. Banu Bahşi and A.Y. Oral, *Opt. Mater. (Amst.)* 29, 672 (2007).
32. I.L. Poul Raj, S. Valanarasu, K. Hariprasad, J.S. Ponraj, N. Chidhambaram, V. Ganesh, H.E. Ali, and Y. Khairy, *Opt. Mater. (Amst.)* 109, 110396 (2020).
33. C. Anastasescu, M. Zaharescu, D. Angelescu, C. Munteanu, V. Bratan, T. Spataru, C. Negrila, N. Spataru, and I. Balint, *Sol. Energy Mater. Sol. Cells* 159, 325 (2017).
34. M.M. Nakata, T.M. Mazzo, G.P. Casali, F.A. La Porta, and E. Longo, *Chem. Phys. Lett.* 622, 9 (2015).
35. M. Hadiyan, A. Salehi, and A. Koohi-Saadi, *J. Electroceram.* 42, 147 (2019).
36. D.P. Joshi and K. Sen, *Sol. Cells* 9, 261 (1983).
37. H. Albargi, Z.R. Khan, R. Marnadu, H.Y. Ammar, H. Algadi, A. Umar, I.M. Ashraf, and M. Shkir, *J. King Saud Univ. Sci.* 33, 101638 (2021).
38. S. Rajeswari, M.M. Ibrahim, A.M. Al-Enizi, M. Ubaidullah, P. Arunachalam, B. Pandit, and S.F. Shaikh, *J. Mater. Sci. Mater. Electron.* 33(24), 19284 (2022).
39. Z.R. Khan, M.S. Revathy, M. Shkir, A. Khan, M.A. Sayed, A. Umar, A.S. Alshammari, S. Vinoth, R. Marnadu, E.S. Yousef, H. Algarni, and S. Al Faify, *Surf. Interfaces* 28, 101586 (2022).
40. S. Veeralingam and S. Badhulika, *J. Alloys Compd.* 885, 160954 (2021).
41. S. Liu, S. Jiao, J. Zhang, H. Lu, D. Wang, S. Gao, J. Wang, and L. Zhao, *Appl. Surf. Sci.* 571, 151291 (2022).
42. S. Dhar, T. Majumder, and S.P. Mondal, *ACS Appl. Mater. Interfaces* 8, 31822 (2016).
43. W. Yin, J. Yang, K. Zhao, A. Cui, J. Zhou, W. Tian, W. Li, Z. Hu, and J. Chu, *ACS Appl. Mater. Interfaces* 12, 11797 (2020).
44. A. Das Mahapatra and D. Basak, *J. Alloys Compd.* 797, 766 (2019).
45. C.C.S. Maria, R.A. Patil, D.P. Hasibuan, C.S. Saragih, C.C. Lai, Y. Liou, and Y.R. Ma, *Appl. Surf. Sci.* 584, 152608 (2022).
46. F.X. Liang, C.W. Ge, T.F. Zhang, W.J. Xie, D.Y. Zhang, Y.F. Zou, K. Zheng, and L.B. Luo, *Nanophotonics* 6, 494 (2017).
47. Y. Liu, P. Chen, G. Dai, W. Su, Y. Sun, J. Hou, N. Zhang, G. Zhao, Y. Fang, and N. Dai, *Phys. E Low Dimens. Syst. Nanostruct.* 120, 114041 (2020).
48. J. Chao, S. Xing, Z. Liu, X. Zhang, Y. Zhao, L. Zhao, and Q. Fan, *Mater. Res. Bull.* 98, 194 (2018).
49. W. Huang, C. Xing, Y. Wang, Z. Li, L. Wu, D. Ma, X. Dai, Y. Xiang, J. Li, D. Fan, and H. Zhang, *Nanoscale* 10, 2404 (2018).

Publisher's Note Springer Nature remains neutral with regard to jurisdictional claims in published maps and institutional affiliations.

Springer Nature or its licensor (e.g. a society or other partner) holds exclusive rights to this article under a publishing agreement with the author(s) or other rightsholder(s); author self-archiving of the accepted manuscript version of this article is solely governed by the terms of such publishing agreement and applicable law.